ACS central science

Research Article

Cite This: ACS Cent. Sci. 2019, 5, 1146–1158

http://pubs.acs.org/journal/acscii

Biowire Model of Interstitial and Focal Cardiac Fibrosis

Erika Yan Wang,[†] Naimeh Rafatian,[‡,§,○] Yimu Zhao,[∥,○] Angela Lee,[⊥] Benjamin Fook Lun Lai,[†] Rick Xingze Lu,[†] Danica Jekic,[#] Locke Davenport Huyer,[†,∥] Ericka J. Knee-Walden,[†] Shoumo Bhattacharya,[⊥] Peter H. Backx,[‡,§,▽] and Milica Radisic*[,†,§,∥]

[†]Institute of Biomaterials and Biomedical Engineering, University of Toronto, Toronto, Ontario M5S 3G9, Canada

[‡]Department of Physiology, Faculty of Medicine, University of Toronto, Toronto, Ontario M5S 1A8, Canada

[§]Toronto General Research Institute, Toronto, Ontario M5G 2C4, Canada

[∥]Department of Chemical Engineering and Applied Chemistry, University of Toronto, Toronto, Ontario M5S 3E5, Canada

[⊥]RDM Division of Cardiovascular Medicine and Wellcome Trust Centre for Human Genetics, University of Oxford, Oxford OX3 7BN, United Kingdom

[#]McGill University, Montreal, Quebec H3A 2K6, Canada

[▽]Department of Biology, York University, Toronto, Ontario M3J 1P3, Canada

Supporting Information

ABSTRACT: Myocardial fibrosis is a severe global health problem due to its prevalence in all forms of cardiac diseases and direct role in causing heart failure. The discovery of efficient antifibrotic compounds has been hampered due to the lack of a physiologically relevant disease model. Herein, we present a disease model of human myocardial fibrosis and use it to establish a compound screening system. In the Biowire II platform, cardiac tissues are suspended between a pair of poly(octamethylene maleate (anhydride) citrate) (POMaC) wires. Noninvasive functional readouts are realized on the basis of the deflection of the intrinsically fluorescent polymer. The disease model is constructed to recapitulate contractile, biomechanical, and electrophysiological complexities of fibrotic myocardium. Additionally, we constructed a heteropolar integrated model with fibrotic and healthy cardiac tissues coupled together. The integrated model captures the regional heterogeneity of scar lesion, border zone, and adjacent healthy myocardium. Finally, we demonstrate the utility of the system for the evaluation of antifibrotic compounds. The high-fidelity *in vitro* model system combined with convenient functional readouts could potentially facilitate the development of precision medicine strategies for cardiac fibrosis modeling and establish a pipeline for preclinical compound screening.

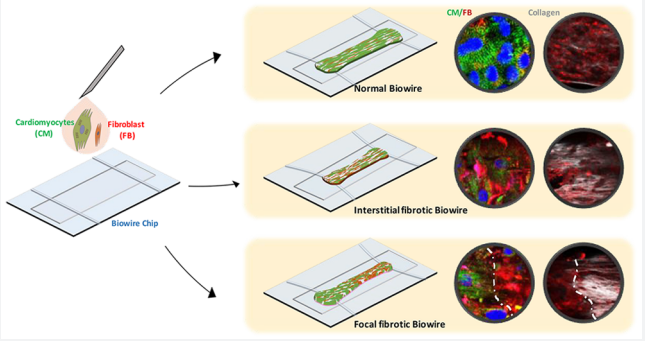

INTRODUCTION

Cardiac fibrosis, also known as myocardial scarring, often results from myocardial infarction (MI) as well as nonischemic cardiomyopathies associated with various gene mutations, pressure overload, aging, and clinical interventions such as ablation.[1] Cardiac fibroblast (cFB) replacement of cardiomyocytes (CMs) and accumulation of extracellular matrix (ECM) is present in nearly all cases of cardiac fibrosis.[1] In the fibrotic myocardium, collagen deposition contributes to reduced diastolic chamber compliance[1] which is associated with the activation of myofibroblasts (myoFBs),[2] a differentiated form of fibroblast which is responsible for dramatically elevating collagen synthesis and further promoting matrix stiffening.[3] Collagen deposition also increases the internal load which leads to deterioration of cardiac contractile force and impairment of systolic function.[4,5]

Another pivotal aspect of the fibrotic myocardium is altered electrophysiology.[6] Fibrosis often associates with arrhythmogenesis and abnormal electrical impulse propagation.[6,7] This can arise both from disruption of electrical coupling between CMs as a result of the creation of conduction barriers by the ECM[1,7] and by the electronic loads placed on CMs coupled electrically to the increased numbers of FBs.[7] The interplay between these effects of fibrosis on cardiac electrophysiology as well as the role of paracrine signaling and other factors remains poorly understood.

To better elucidate the disease mechanisms and develop therapeutic strategies, an ideal model of cardiac fibrosis should exhibit the hallmarks of disease.[5] Conventional use of monolayer cell cultures cannot easily capture the structural and functional properties of fibrotic myocardium due to the oversimplification of the extracellular microenvironment.[8] The "scar-in-a-jar" model is a well-validated *in vitro* system to study

Received: January 18, 2019
Published: June 4, 2019

DOI: 10.1021/acscentsci.9b00052
ACS Cent. Sci. 2019, 5, 1146–1158

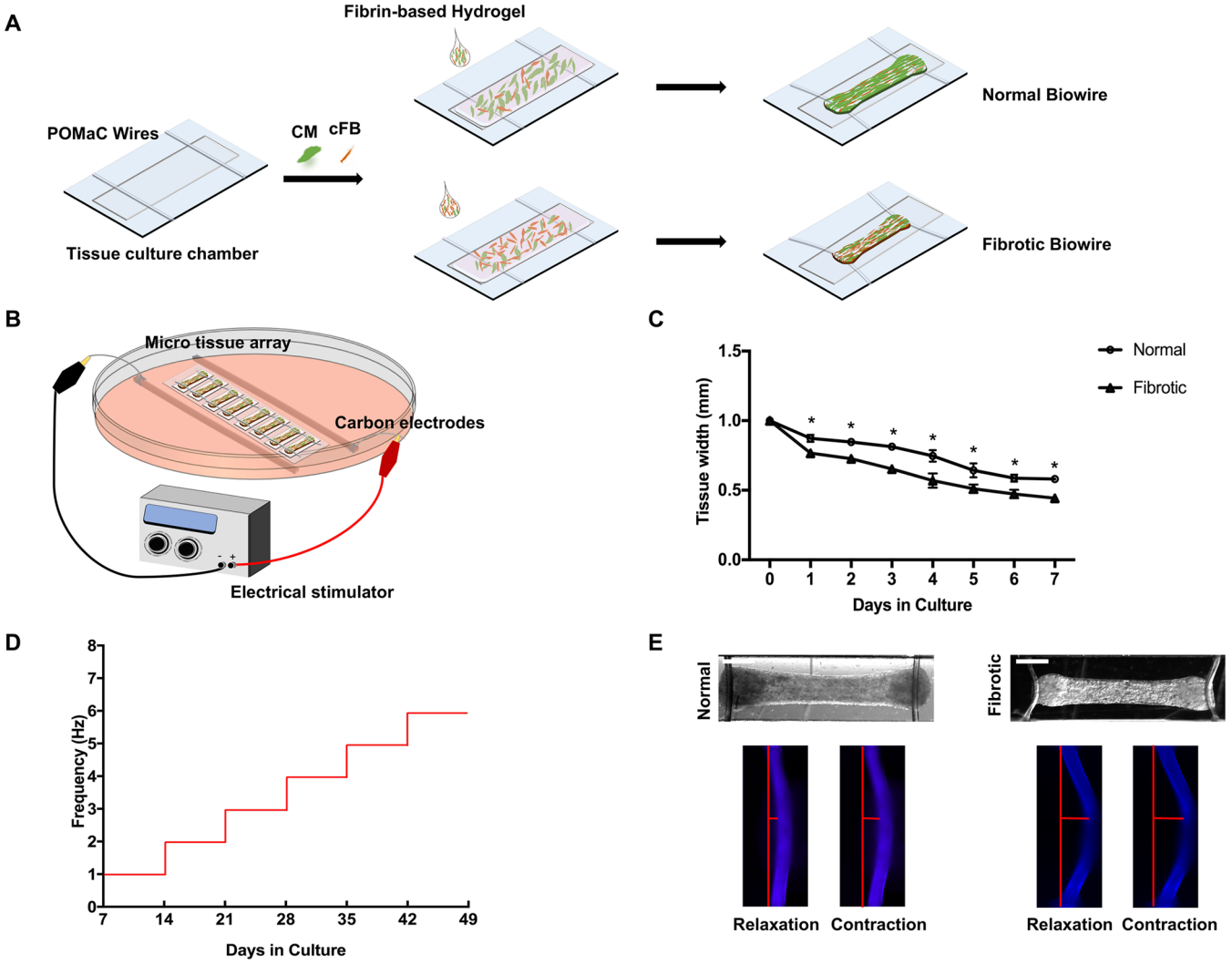

Figure 1. Generation of the disease model on the Biowire II platform. (A) Schematic of the Biowire II chip design and tissue construction. (B) Schematic of the electrical stimulation chamber for tissue maturation. (C) Quantification of compaction based on the tissue width measurement during the first 7 days of culture (mean ± SD, n = 3, one-way repeated measures ANOVA within each group). (D) Protocol used to electrically condition tissues upon compaction to promote tissue organization and maturation. (E) Representative bright field images of normal and fibrotic tissues and intrinsically fluorescent POMaC wires observed under blue fluorescent light as the tissues undergo relaxation−contraction cycles. Wire bending due to passive tension and the maximum active force development generated by the tissues are illustrated with the red bars. (Scale bar = 500 μm).

the biosynthetic cascade of collagen matrix formation underlying fibrosis.[9] However, this model is composed of fibroblasts alone and does not reflect the physiological cellular diversity in the native heart.

Organ-on-chip platforms have recently emerged as biomimetic systems for elucidating human disease *in vitro*.[8,10] Several tissue models of myocardial fibrosis have been reported.[11−14] A simplified 3D cardiac fibrotic model was constructed by encapsulating CMs and cardiac FBs within a mechanically engineered gelatin methacryloyl hydrogel to recapitulate a fibrogenic microenvironment.[12] Another fibrotic model was created via modulation of CM and myoFB volume fractions and showed the effects of cellular composition on impulse conduction velocity.[13] Membranous microtissues were also cultivated with FB-populated collagen matrix to recapitulate biomechanical properties and morphological change in healthy and fibrotic tissues.[14] These systems contain more authentic biomechanical cues for disease modeling than a thin layer of cells. However, these engineered constructs can only partially match the electrophysiological properties and contractile functions in human myocardium. The focus on electrophysiological remodeling is particularly lacking.

Our group previously developed Biowire, a heart-on-a-chip platform for cultivating miniaturized engineered cardiac tissues with authentic adult human myocardial phenotypes.[15] An extension of this technique called the Biowire II platform involved the generation and long-term culturing of cylindrical tissues resembling human trabeculae that are suspended between two poly(octamethylene maleate (anhydride) citrate) (POMaC) wires.[16] This platform uses the deflection of POMaC wires to continuously and reliably measure absolute contractile systolic and diastolic properties,[16] thereby allowing real-time readouts of active force, passive tension, Ca^{2+} transients, and electrical properties.

Using this platform, we present a disease-on-a-chip model exhibiting biomechanical and electrophysiological features of fibrotic cardiomyopathy in the adult human heart. This platform enables structural and functional maturation of

DOI: 10.1021/acscentsci.9b00052
ACS Cent. Sci. 2019, 5, 1146−1158

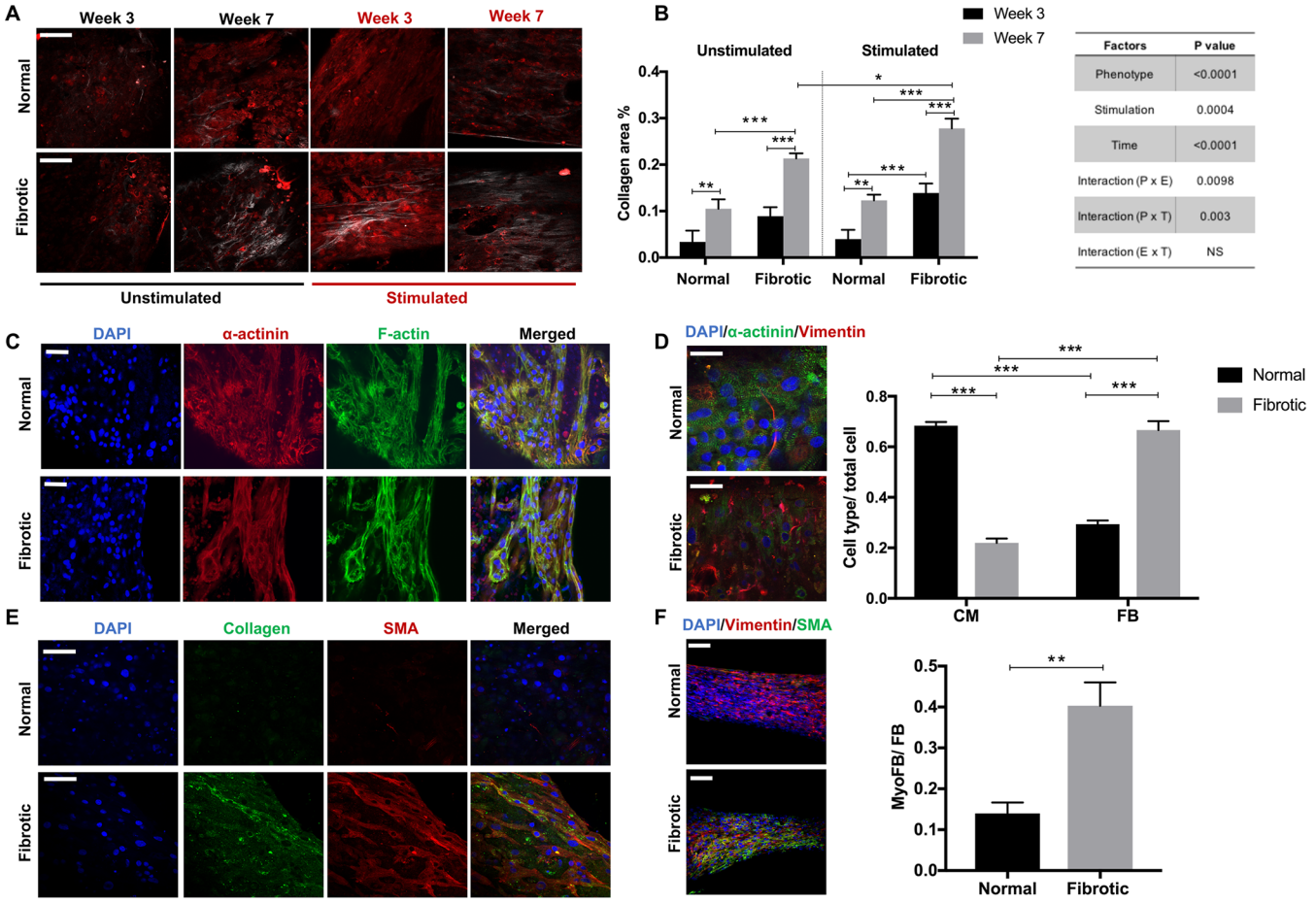

Figure 2. Fibrotic tissues exhibit enhanced collagen deposition and elevated myofibroblast content. (A, B) Representative secondary harmonic generation (SHG) images and quantification of collagen content in normal and fibrotic tissues measured at week 3 and 7 of cultivation. Stimulated is the group subjected to electrical conditioning during cultivation. Unstimulated is the control. Scale bar = 100 μm (mean ± SD, $n \geq 3$, three-way ANOVA). The table show results of three-way ANOVA. (C) Representative immunostaining images of normal and fibrotic tissues at the stimulation end point stained for filamentous actin (F-actin) cytoskeleton and sarcomeric α-actinin and counterstained with the nuclear stain DAPI. Scale bar = 100 μm. (D) Representative immunostaining images of normal and fibrotic tissues at stimulation end point double-stained for vimentin and sarcomeric α-actinin and counterstained with the nuclear stain DAPI (scale bar = 50 μm). CM and cFB number are normalized to the total cell count at the tissue cultivation end point (mean ± SD, $n \geq 3$, two-way ANOVA). (E) Representative immunostaining images of normal and fibrotic tissues at the stimulation end point stained for collagen type I and α-smooth muscle actin (α-SMA) and counterstained with the nuclear stain DAPI (scale bar = 50 μm). (F) Representative immunostaining images of normal and fibrotic tissues at the stimulation end point double-stained for vimentin and α-SMA and counterstained with the nuclear stain DAPI (scale bar = 100 μm). myoFB fraction in the total fibroblast population (mean ± SD, $n = 3$, Student's t test).

three-dimensional constructs with electrical conditioning. By taking advantage of the ability to generate heteropolar Biowires,[16] we further tested the feasibility of engineering a scar-myocardium integrated model to mimic the interaction between scar lesion and adjacent healthy tissue. To our knowledge, this is the first mechanoelectrically coupled scar-on-a-myocardium model with fibrotic and healthy myocardial tissues growing together. Characterizations can be performed on both normal and fibrotic sides as well as the interface to elucidate structural and functional modifications in the scar-affected myocardium.

The main value of developing organ-on-a-chip models for human disease is in the ability to evaluate drugs. The Biowire II platform enables the screening of antifibrotic compounds noninvasively on the basis of tissue contractility and compaction without disturbing long-term tissue cultivation. Potential drug candidates can be primarily screened on the basis of their ability to attenuate passive tension and further evaluated by their ability to inhibit collagen deposition.

Proprotein convertases (PCSKs) are a family of serine proteases that cleave secreted peptides.[17] PCSKs have been reported to be involved in heart failure and intimal hyperplasia through the activation of the TGF-β/Smad signaling pathway.[17] Furin is one of the most ubiquitously expressed PCSKs; thus, it may be a potential therapeutic target in fibrosis.[17,18] Herein, we use a commercially available furin inhibitor as a model compound to demonstrate the utility of the Biowire II platform in selecting antifibrotic drug candidates.

RESULTS

Construction of Cardiac Fibrosis-on-a-Chip. The Biowire II platform consists of an array of microchambers fitted with two polymer (POMaC) wires (Figure 1A). The microchambers are created on a polystyrene base using microfabrication and hot embossing techniques as previously reported.[16,19] The cellular composition and mechanical properties of the tissues are tailored by systematically

DOI: 10.1021/acscentsci.9b00052
ACS Cent. Sci. 2019, 5, 1146−1158

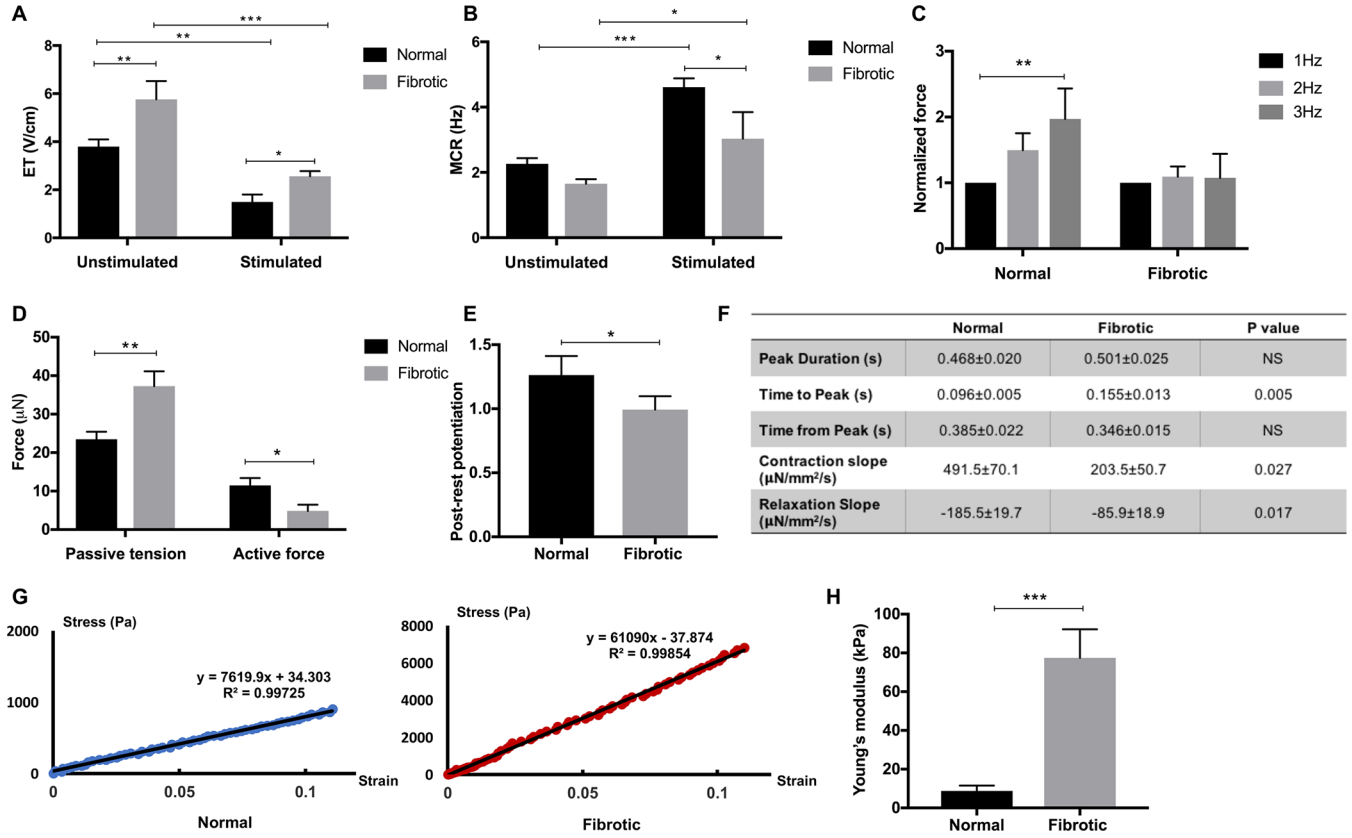

	Normal	Fibrotic	P value
Peak Duration (s)	0.468±0.020	0.501±0.025	NS
Time to Peak (s)	0.096±0.005	0.155±0.013	0.005
Time from Peak (s)	0.385±0.022	0.346±0.015	NS
Contraction slope (μN/mm²/s)	491.5±70.1	203.5±50.7	0.027
Relaxation Slope (μN/mm²/s)	-185.5±19.7	-85.9±18.9	0.017

Figure 3. Fibrotic tissues exhibit inferior contractile properties compared to the controls. (A, B) Excitation threshold (ET) and maximum capture rate (MCR) measurements for the normal and fibrotic tissues cultivated with (stimulated) or without (unstimulated) electrical conditioning (mean ± SD, $n \geq 3$, two-way ANOVA). (C) Active force of normal and fibrotic tissues when stimulated from 1 to 3 Hz (mean ± SD, $n \geq 3$, one-way ANOVA within each group). (D) Passive tension and active force for the normal and fibrotic tissues at the electrical conditioning end point (mean ± SD, $n = 3$, Student's t test within each group). (E) Postrest potentiation (PRP) of force (normalized to the last pacing frequency) in both groups at the end point of electrical conditioning (mean ± SD, $n \geq 3$, Student's t test). (F) Quantification of force dynamics (mean ± SD, $n \geq 3$, Student's t test). (G) Representative stress−strain relationship for the Young's modulus in each group. The experimental data are from the linear regions of stress−strain curves obtained by the MicroSquisher stretching test. (H) Young's moduli of normal and fibrotic tissues at the end of electrical conditioning (mean ± SD, $n \geq 3$, Student's t test).

manipulating the cell populations in a tuned hydrogel. Cardiomyocytes derived from human induced pluripotent stem cells (hiPSC-CMs) are cocultured with either 25% or 75% ventricular cardiac fibroblasts to model normal and fibrotic myocardium, respectively (Figure 1A). A fibrin-based hydrogel is used to encapsulate the cells according to a composition recently reported to enable the creation of a highly mature ventricular myocardium.[20] The hydrogel is prepared with minimal collagen content to facilitate the accurate measurement of collagen deposition.

Once assembled, the Biowire tissues undergo a process of gel compaction over the next 7 days, wherein the ECM becomes more structured and dense with compaction being more rapid and pronounced in the fibrotic (75% fibroblasts) tissues compared to the control tissues (Figure 1C).

Since electrical conditioning improves cardiac tissue function and maturation,[21] we routinely applied chronic electrical stimulation to our tissues using carbon rods (Figure 1B) after tissue compaction, with the stimulation frequency increasing by 1 Hz each week for the next 6 weeks[16] (Figure 1D). During the entire culture period, muscle contraction and relaxation can be quantified from the deflection of the POMaC wire associated with electrical field stimulation (Figure 1E). Notably, these measurements reveal, as might be expected, that the passive tension is greater in the fibrotic tissues compared to the normal tissues (Figure 1E).

Compositional Remodeling and Collagen Deposition in the Fibrotic Disease Model. Second harmonic generation (SHG) imaging is performed to provide information on collagen content and structural modification (Figure 2A). A more than 2-fold increase of collagen content in the fibrotic tissues compared to the normal tissues is observed by the end of electrical conditioning (Figure 2B). In addition to a more abundant collagen content, electrically conditioned groups also present a more aligned collagen structure (Figure 2A,B). Collagen bundles reportedly have an anisotropic architecture in the healthy heart, whereas they often appear densely packed in parallel configurations in fibrotic tissues.[22] To demonstrate that collagen remodeling is similar to *in vivo* fibrotic lesions, cardiac sections from postmyocardial infarction (MI) rat hearts are imaged as a comparison (Figure S8). The comparable collagen structure is visualized in the Biowire tissues and fibrotic heart sections, indicating the similarity of the Biowire fibrotic tissue to a real cardiac scar. Numerous collagen fibers are diffusely present in the MI heart, whereas minimal fibrillar collagen accumulation is observed in the sham group, except for a few thin fibers. The presence of focal fibrosis is also observed in the MI heart, characterized by the localized distribution of excessive collagen (Figure S8).

DOI: 10.1021/acscentsci.9b00052
ACS Cent. Sci. 2019, 5, 1146−1158

A

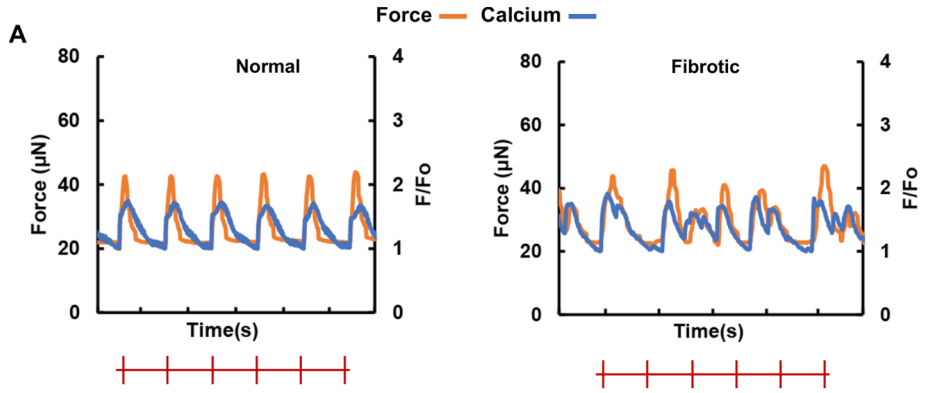

B

	Normal	Fibrotic	P value
Amplitude (dF/Fo)	0.987 ± 0.208	0.224 ± 0.064	0.013
Peak Duration (s)	0.798 ± 0.187	0.304 ± 0.038	NS
Time to Peak (s)	0.069 ± 0.005	0.115 ± 0.011	0.020
Time from Peak (s)	0.641 ± 0.095	0.222 ± 0.059	0.020
Rising slope (dF/Fo/s)	8.323 ± 1.817	1.471 ± 0.349	0.021
Tau decay (s)	0.370 ± 0.013	0.179 ± 0.022	0.002

Figure 4. Fibrotic tissues exhibit abnormal calcium transients and electrophysiological properties compared to the controls. (A) Representative active force (orange) and calcium transient (blue) traces of normal and fibrotic electrically conditioned tissues under electrical field stimulation at 1 Hz. The red marks indicate pacing frequency. (B) Quantification of the calcium transient properties (mean ± SD, $n \geq 3$, Student's t test).

These results support the use of electrical stimulation in the disease modeling system. The fibrotic tissues present the disrupted organization of the myofibril ultrastructure compared to normal tissues, visualized by the filamentous actin (F-actin) cytoskeleton and sarcomeric α-actinin staining (Figure 2C). In the human heart, cardiomyocytes contain highly organized sarcomeres with a length up to ~2.2 μm.[23] Average sarcomere lengths of 2.0 ± 0.01 and 1.9 ± 0.02 μm were observed in normal and fibrotic Biowire tissues, which are both within the range of the sarcomere length of adult cardiomyocytes (Figure S6A,B). Costaining for α-actinin and vimentin is used to quantify the ratio of CMs to nonmyocytes at the tissue cultivation end point. There is no dramatic change in the cFB/CM ratio compared to the initial seeding composition (Figure 2D), demonstrating that the Biowire II platform provides a relatively stable microenvironment for maintaining FB quiescence compared to the flat plastic surfaces of traditional tissue culture plates.[24] Staining for myofibroblasts (myoFBs) marked by α-smooth muscle actin (α-SMA) indicates that myoFBs are abundant in the fibrotic tissues but minimally present in healthy controls (Figure 2E). The fibrotic tissues are composed of living myoFBs embedded in deposited collagen (Figure 2E). More than a 3-fold increase in the myoFB ratio is observed in the fibrotic tissues compared to the normal tissues (Figure 2F). The distribution of the Connexin 43 (Cx43) gap-junction protein exhibits a relatively uniform pattern in the normal Biowire tissues, whereas a marked disruption of Cx43 distribution is observed in the fibrotic tissues (Figure S7).

Fibrotic Tissues Exhibit Deteriorating Contractile Function Compared to the Healthy Tissues. We also performed multiparametric assessments to further assess the properties of our engineered Biowire II tissues after 7 weeks of maturation. As reported previously,[16] electrical conditioning reduces the excitation threshold (ET) voltage needed to initiate contraction and increases the maximum capture rates (MCRs) for both normal and fibrotic tissues (Figure 3A,B). However, fibrotic tissues generally require higher ETs and displayed lower MCR than the normal tissues, suggesting impaired electrical integrity (Figure 3A,B). Moreover, after 6 weeks of electrical stimulation, normal tissues have pronounced positive force−frequency relationships (FFRs) (Figure 3C and Figure S1), indicative of enhanced maturation.[16] Despite improvements in contractility and excitability observed with electrical conditioning, the FFR at the end of cultivation is flatter (Figure 3C and Figure S1), and the postrest potentiation (PRP) of force is less pronounced in fibrotic tissues compared to normal Biowire II tissues (Figure 3E).

Consistent with the impaired systolic and diastolic function typically seen in cardiac fibrosis, fibrotic tissues exhibit both diminished active contractile force and increased passive tension (Figure 3D), accompanied by the prolonged time to peak in active force development in the fibrotic group compared to the normal group, despite comparable transient

DOI: 10.1021/acscentsci.9b00052
ACS Cent. Sci. 2019, 5, 1146−1158

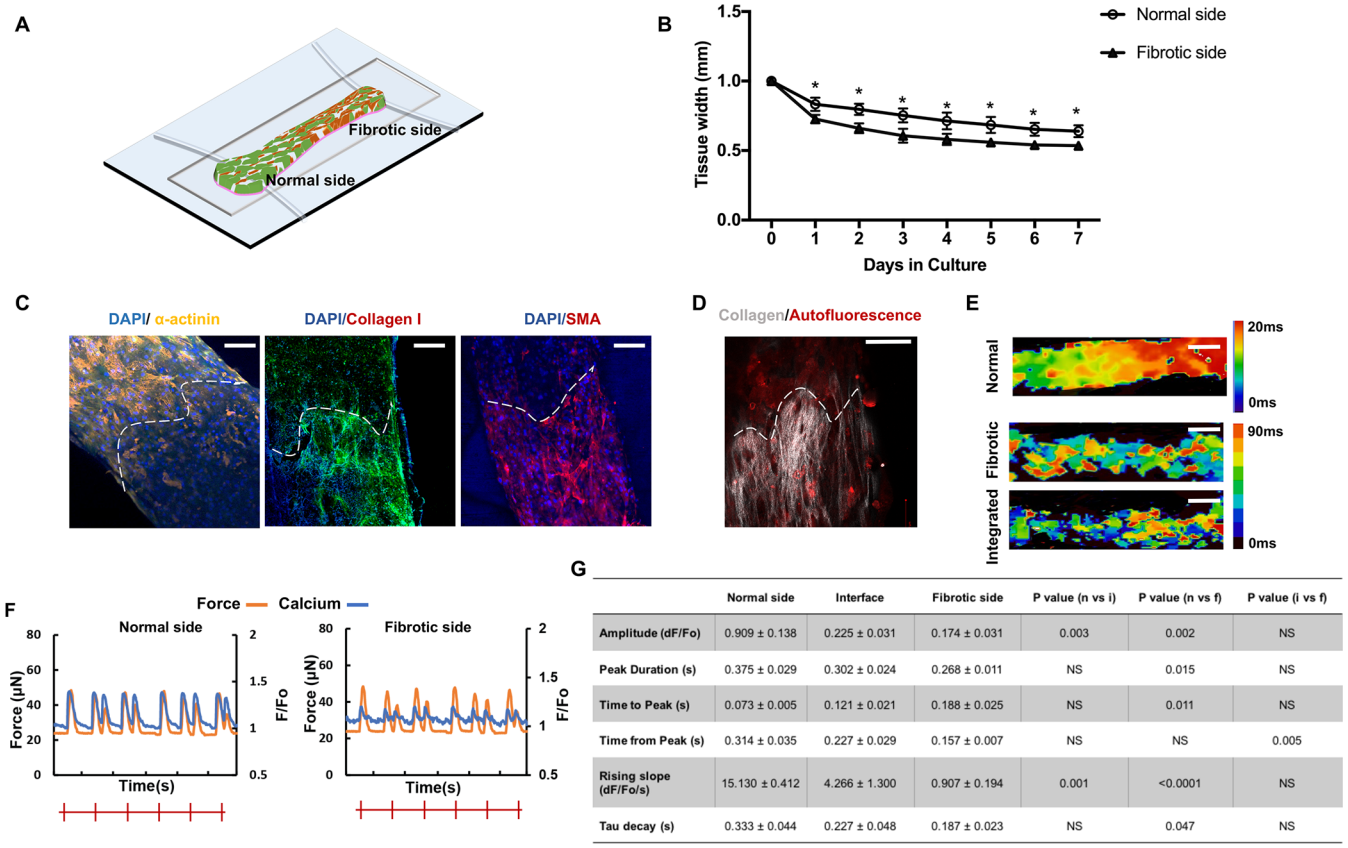

	Normal side	Interface	Fibrotic side	P value (n vs i)	P value (n vs f)	P value (i vs f)
Amplitude (dF/Fo)	0.909 ± 0.138	0.225 ± 0.031	0.174 ± 0.031	0.003	0.002	NS
Peak Duration (s)	0.375 ± 0.029	0.302 ± 0.024	0.268 ± 0.011	NS	0.015	NS
Time to Peak (s)	0.073 ± 0.005	0.121 ± 0.021	0.188 ± 0.025	NS	0.011	NS
Time from Peak (s)	0.314 ± 0.035	0.227 ± 0.029	0.157 ± 0.007	NS	NS	0.005
Rising slope (dF/Fo/s)	15.130 ± 0.412	4.266 ± 1.300	0.907 ± 0.194	0.001	<0.0001	NS
Tau decay (s)	0.333 ± 0.044	0.227 ± 0.048	0.187 ± 0.023	NS	0.047	NS

Figure 5. Construction and characterization of the scar-myocardium integrated model. (A) Schematics of the integrated scar-myocardium model. A model of focal fibrosis is generated by seeding a normal (25%) and a high (75%) percentage of FBs together with CMs at the opposing ends of the Biowire II tissue. (B) Quantification of compaction based on the tissue width measurement on the two opposing sides of the integrated tissue during the first 7 days of culture (mean ± SD, $n \geq 3$, one-way repeated measures ANOVA within each group). (C) Representative immunostaining images of the integrated tissue stained for sarcomeric α-actinin, collagen type I, and α-SMA. The dashed lines mark the geometrical segregation at the interface (scale bar = 100 μm). (D) SHG imaging of collagen. The dashed lines mark the geometrical segregation at the interface (scale bar = 100 μm). (E) Conduction velocity maps for normal, fibrotic, and integrated tissues (scale bar = 500 μm). The color scale represents the time for an electrical pulse to pass through in milliseconds. (F) Representative active force (orange) and calcium transient (blue) traces of normal and fibrotic sides on the same integrated tissue under electrical field stimulation at 1 Hz. (G) Corresponding quantification of calcium transients on the opposing sides of the tissues and the interface (mean ± SD, $n \geq 3$, one-way ANOVA).

durations (Figure 3F). Consistent with our previous findings and the analysis of the published results we provided previously,[16] both normal and fibrotic Biowire II tissues exhibit active forces that are lower compared to those reported previously,[20,25−27] but when normalized to the input CM number, the forces are comparable in this work and previous studies[15,16] (Figure S6C). In addition, Young's moduli of normal and fibrotic tissues are in agreement with the mechanical properties reported in the healthy (Young's modulus ∼10 kPa) and fibrotic (2−10 times stiffer) human myocardium, respectively[28] (Figure 3G,H).

Although most of the results here are obtained using BJ1D iPSC-derived cardiomyocytes, the fibrotic tissues can be constructed in the Biowire II platform using a commercially available cell source iCell cardiomyocytes (Figure S2).

Abnormal Calcium Handling and Electrophysiological Properties Present in the Fibrotic Tissues. Modifications in calcium transients, excitation−contraction coupling, and electrical properties are also observed in the fibrotic tissues compared to the normal tissue. Specifically, calcium transient amplitudes are lower with greater amounts of unsynchronized calcium waves in fibrotic tissues (Figure 4A). In addition, the rising slope of calcium transients and the relaxation time constant are smaller in the fibrotic compared to the normal tissues (Figure 4B). Despite abbreviated calcium transients, the time to peak is significantly longer in the fibrotic compared to the normal tissue (Figure 4B). Arrhythmic beating is also observed in all fibrotic tissues through calcium tracing and optical mapping (Figure 4A).

Altered action potential profiles, including depolarization of cardiomyocyte resting potential, reduction of cardiomyocyte maximum upstroke velocity, and prolonged cardiomyocyte action potential duration, are observed in the fibrotic model (Figure S3).

Construction of the Scar-Myocardium-Integrated-Model-on-a-Chip. With the aim to construct a disease model recapitulating scar lesion integration on the normal myocardium, we spatially patterned normal and fibrotic tissues to generate a heteropolar model with both compartments (Figure 5A). While growing together and beating synchronously upon compaction, intrinsic morphological and functional properties that are seen in individual fibrotic or normal tissues are still present at the opposing sides of a single Biowire II tissue. The fibrotic side shows faster and denser compaction as seen individually (Figure 5B). A defined geometrical segregation of cellular composition, collagen-dense area, and

DOI: 10.1021/acscentsci.9b00052
ACS Cent. Sci. 2019, 5, 1146−1158

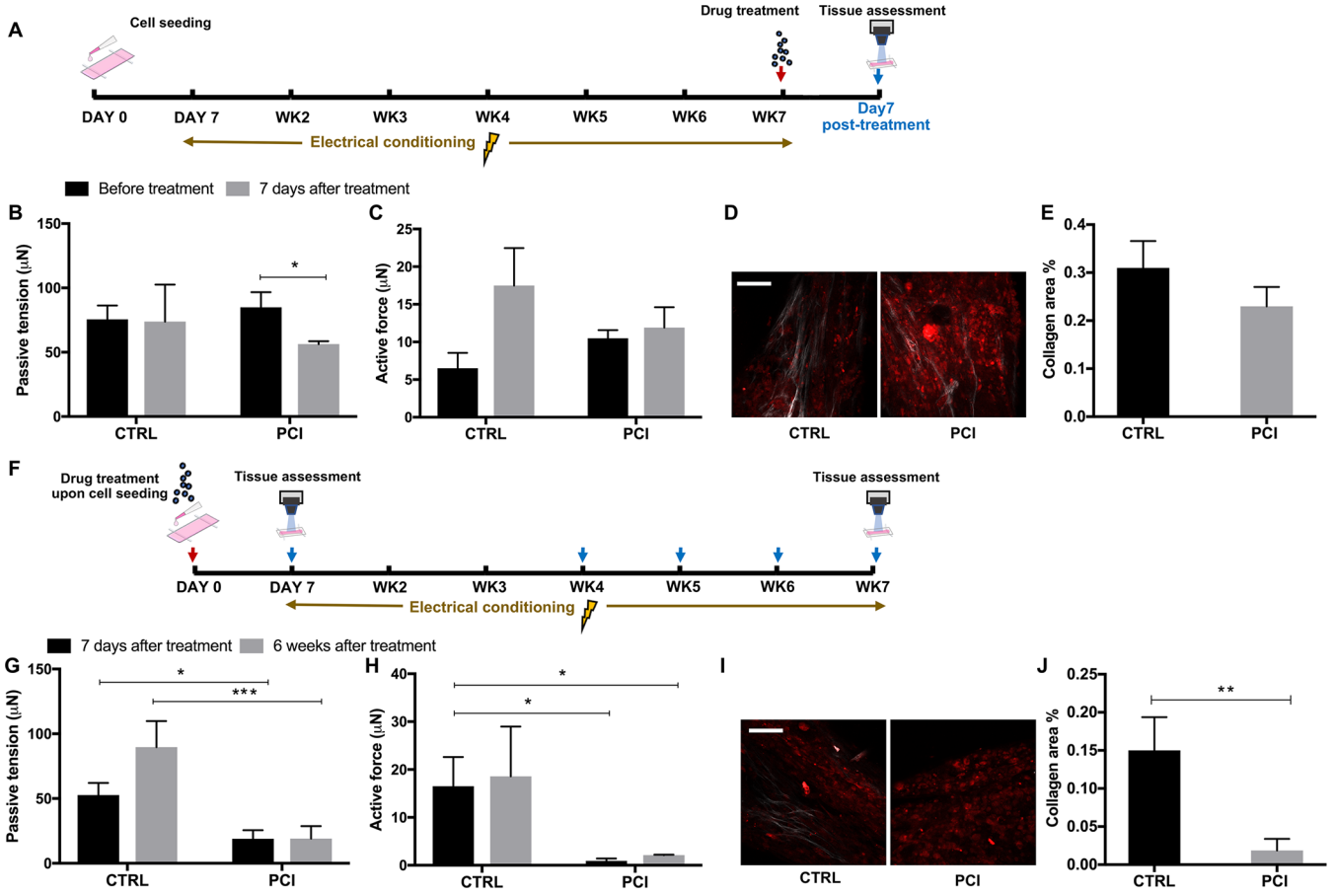

Figure 6. Proof of concept drug screening. (A) Schematic of the drug screening timelines of the late treatment (Regimen 1). (B, C) Passive tension and active force before and after 7 days of PCI treatment with matured fibrotic tissues based on Regimen 1 (mean ± SD, $n = 3$, Student's t test within each group). (D) Representative SHG images of fibrotic tissues treated with PCI for 7 days compared to the DMSO control (scale bar = 100 μm). (E) Corresponding quantification of the collagen area ratio (mean ± SD, $n \geq 3$, Student's t test). (F) Schematic of the drug screening timeline of the early treatment (Regimen 2). (G, H) Passive tension and active force after 7 days and 6 weeks of PCI treatment based on Regimen 2 (mean ± SD, $n = 3$, two-way ANOVA). (I, J) Representative SHG images (scale bar = 100 μm) and corresponding quantification of fibrotic tissues treated with PCI for 7 days based on Regimen 2 (mean ± SD, $n \geq 3$, Student's t test).

myoFB activation are visualized by immunostaining for α-actinin, collagen I, and α-SMA as well as SHG imaging (Figure 5C,D).

Contractile and electrophysiological properties are evaluated with the integrated model as important indicators of the scar-myocardium interaction. Impulse propagation velocity diminishes, and arrhythmia appears at the normal side of the heteropolar tissue, due to the conduction block created by the fibrotic side of the integrated model (Figure 5E). Excitation–contraction coupling clearly displays different profiles at the fibrotic and normal sides (Figure 5F,G). Through calcium tracing and optical mapping, arrhythmic waves are observed across the integrated tissue, especially in the interface region where two compartments are connected (Figure 5E,F). Calcium transients are faster with a larger amplitude at the normal side compared to the interface and the fibrotic side of the integrated mode (Figure 5G). However, when a comparison is made to the normal single tissue, it is clear that both systolic and diastolic properties of the normal side are inferior in the integrated tissues compared to the single normal tissues (Figure 5G).

Drug Testing with Fibrotic Biowire II Tissues. Increased passive tension is a suggested mechanism underlying diastolic dysfunction in cardiac fibrosis.[24,29,30] Passive tension of the myocardium is affected by CM titin properties and extracellular collagen.[29,30] Thus, Biowire screening uses passive tension as the primary screening parameter. SHG collagen imaging and tissue compaction data are obtained as validation tools to evaluate the antifibrotic effect. The direct readout of active force, ET, and MCR is used to monitor cardiac tissue contractility and electrical integrity after drug treatment without disturbing tissue cultivation.

We first compared the efficacy of three commercially available furin inhibitors in reducing collagen deposition using a 96-well plate "scar-in-a-jar" model, including p-guanidinomethyl-phenylacetyl-Arg-Val-Arg-4-amidinobenzylamide (PCI), dec-RVKR-cmk (FiI), and hexa-D-arginine amide (FiII). PCI showed the most potent efficacy in reducing reticular collagen deposition among the three compounds (Figure S4A). The inhibition is specific to collagen and does not affect other major ECM proteins such as fibronectin (Figure S4B). Therefore, PCI is selected as the model compound to be used in Biowire drug testing.

Considering the time-dependent nature of collagen deposition, two different regimens for the treatment of Biowire II tissues with PCI, late versus early, are investigated (Figure 6A,F). With the first regimen, fibrotic tissues undergo electrical conditioning for 6 weeks to establish mature fibrotic

DOI: 10.1021/acscentsci.9b00052
ACS Cent. Sci. 2019, 5, 1146–1158

phenotypes before compound treatment (Figure 6A). This regimen aims to screen antifibrotic effects on tissues with established pathological phenotypes. Significantly alleviated passive tension is observed at 7 days after treatment with PCI (Figure 6B). The treatment has no significant effect on active tension compared to the control group (Figure 6C). Collagen content reduction is observed, albeit at an insignificant level with the PCI treated group compared to the dimethyl sulfoxide (DMSO) treated control (Figure 6D,E). The data suggest no significant drug effects on ET, while elevated MCR is observed in the PCI treated group (Figure S5A).

With the second regimen, the drug effects are assessed on early stage scar formation (Figure 6F). PCI treatment initiated upon cell seeding contributes to the deceleration of tissue compaction (Figure S5B). Correspondingly, reduced passive tension is observed after 7 days of treatment. This effect is maintained in the long-term culture for up to 6 weeks (Figure 6G). The early treatment results in a potent reduction of collagen content (Figure 6I,J). However, a remarkably diminished active tension (Figure 6H) and lower MCRs (Figure S5C) are accompanied by long-term, 6 week PCI treatment. This is presumably due to the diminished intracellular coupling caused by the reduction of cell-gel compaction.

DISCUSSION

In this work, a high-fidelity model of cardiac fibrosis is constructed on the Biowire II system. This disease model enables systematic control and quantification of tissue composition, collagen content, and mechanical properties. Hallmarks of fibrotic myocardium such as myofibroblast activation, tissue stiffening, impaired contractile and electrical properties, and concomitant arrhythmogenesis are exhibited in this disease model.

The tissue construction strategy aims to reproduce the microenvironment involved in most forms of fibrosis, where the elevated presence of cFB takes place after CM loss, and local collagen deposition emerges from the initially homogeneous FB population.[30,31] Overpopulated FBs cause enhanced collagen content and tissue stiffening, which in turn activates myofibroblast differentiation and aggravates collagen deposition; thus, fibrosis is mediated by a self-reinforcing positive-feedback loop.[31] There are several existing fibrotic disease models that depend on exogenous TGF-β and ischemic stimuli.[12,32−34] However, the introduction of exogenous TGF-β can confound the investigation of the endogenous TGF-β pathway. In addition, considering the functional pleiotropy of TGF-β in a wide variety of complex biological processes,[5,35] the current model avoids unpredictable off-target effects and provides a consistent model system easy to reproduce.

Although fibrosis has been intensively studied, the mechanisms responsible for this disease remain unclear. It is difficult to systematically study remodeling due to disease, especially abnormal electrophysiological properties in a monolayer cell culture or 2D planar surface without the intricate electromechanical microenvironment and cell−cell as well as cell−matrix interactions.[36,37] Despite the fact that FBs and myoFBs have multiple ion channels and are able to electrically couple with CMs,[36−39] they are electrically nonexcitable and cannot maintain action potential propagation on their own.[36] We are able to simulate electrophysiological phenomena including reduced conduction velocity propagation, abnormal calcium handling, and altered action potential profiles on a 3D Biowire II chip. By simultaneously measuring calcium transient and contractile force, diminished excitation−contraction coupling is shown in the fibrotic tissues. Action potential profiles vary in different regions of heart.[40] For example, the plateau phase is pronounced in midmyocardium but minimal in endocardium.[40] Action potential duration (APD) has been reported to be in the range 250−400 ms in adult human ventricles.[39,41] The value varies between individuals and the region of the heart being recorded.[41] It is still a challenge to achieve tissue maturation that matches the adult heart in every aspect;[23] therefore, deviation from reported adult APD is expected. The altered action potential components such as hypopolarized membrane potential, decreased AP amplitude, and extended action potential duration (APD) are within the reported range for stem-cell-derived cardiac tissues[16,20] and in accordance with previously reported studies.[42,43] Abnormal calcium handling indicated by diminished calcium intensity and elongated time to peak is also in line with clinical findings with failing fibrotic hearts.[38,44] Moreover, the FFR data are in agreement with previous studies of force production in human myocardium, showing that there is a positive frequency treppe in normal myocardium but not in the failing myocardium.[45] FFR indicates the normal positive inotropic response to elevated stimulation frequency and normally appears to be positive in healthy myocardium.[46,47] However, in the failing heart, the frequency treppe is either absent or attenuated at high stimulation frequencies.[48]

The major novelty of this work includes the integrated scar-myocardium model that aims to recapitulate localized cardiac scars that often take place postinfarction.[49−51] There are limited studies targeting the regional remodeling in the fibrotic myocardium. This model provides a feasible tool for studying a small scar region, i.e., focal fibrosis, and scar border zone in an interconnected electrophysiological system. The two tissue compartments in the integrated scar-myocardium model preserve functional and compositional heterogeneity when they grow concurrently. The occurrence of arrhythmia is observed across the tissue. This is in agreement with previous MRI-based studies implicating arrhythmogenic properties of scar lesion and border zone regions.[50,51] The underlying mechanisms have not yet been fully elucidated. The further investigation of electromechanical coupling of the scar tissue and adjacent myocardium with this model can lead to a deeper understanding of fibrosis-associated arrhythmia and potentially facilitate the development of novel therapies aimed at modifying scar properties.

Ideally, human tissues should be used to inform the changes in gene and protein expression in the context of disease, to enable the identification of new drug targets. However, obtaining such information in the context of heart disease is remarkably difficult as both healthy and diseased viable human heart tissue is extremely scarce.[52] The Biowire II fibrotic model is constructed in a high-content format and manufactured with inert materials that are compatible with the industrial standards, which makes it a desirable *in vitro* testbed. The capability of maintaining a long-term culture allows screening at variable time points and maximizes high-content assessments with each tissue. Although it takes 7 weeks to grow the tissue, the cultivation pipeline is established, so tissues are available every day for testing.

By evaluating the antifibrotic efficacy of the small-molecule inhibitor of proprotein convertase furin, we show the potential application of the Biowire II platform in preliminary

DOI: 10.1021/acscentsci.9b00052
ACS Cent. Sci. 2019, 5, 1146−1158

compound screening. Furin expression is known to be increased in the failing heart.[17,18] It is believed to cleave and activate a number of cardiac profibrotic peptides including TGFβ, subsequently switching on signaling pathways linked to cardiac fibrosis.[17] Our results indicate that furin inhibition by PCI attenuates collagen deposition in fibrotic Biowires. The rationale for prescreening with the monolayer "scar-in-a-jar" assay was provided by our recent paper that illustrates the concept of prescreening dozens of kinase inhibitors in monolayers, followed by the neural network facilitated selection of candidates for screening in the Biowire system.[53] In addition, the "scar-in-a-jar" model is a well-validated *in vitro* system to study the collagen matrix.[9] The screening outcome is consistent with the "scar-in-a-jar" assay but provides a higher-content result as it enables collagen content measurement together with functional characterization. The question of when to start antifibrotic treatment is debated;[5,54] therefore, we did not know the optimal time point before the experiment was conducted. As this work aims to provide exploratory data and an appropriate model system for a subsequent larger-scale screening, we chose the two extremes that would bound the space of possible time points. The result suggests that blocking the furin pathway at earlier time points is more effective in prohibiting fibrosis formation and collagen deposition. However, this could be accompanied by detrimental effects on cardiac contractility and electrical integrity, given that collagen deposition is beneficial for the development of cardiac function. The result might provide useful information for future mechanistic studies on pathways related to early fibrosis onset and development. All together, these results indicate the potential utility of this platform in selecting drug candidates and navigating efficient screening timelines, which cannot otherwise be achieved with monolayer culture. As a proof of concept study, concentration gradient and dose−response curves are not included in this preliminary screening. However, the result provides exploratory data for a subsequent intensive screening with larger sample size, dose gradients, and differential timelines.

In summary, the Biwoire II platform is able to capture the complex physiological and pathological cues of the fibrotic human myocardium. A highly physiologically relevant fibrotic myocardial model and healthy control can be reproduced as distinct constructs and integrated together. In conjunction with previous functional and proteomics studies, this high-content label-free system can be used as a promising tool to perform predictive and informative drug screening for preclinical studies. The integrated disease model can potentially allow the precise testing of differential drug responses in scar and healthy tissues as well as enable the assessment of regional remodeling over time.

However, we recognize some limitations of this fibrotic model. It solely recapitulates progressive myoFB activation and fibrosis caused by overpopulated resident fibroblasts. In many cases of cardiac fibrosis, myofibroblasts arise from a variety of origins and present phenotypic heterogeneity in healthy and diseased hearts.[55] Future studies with preconditioned myoFB subtypes as well as factors that regulate myoFB activation will facilitate the development of more physiologically biomimetic models. The construction of the focal fibrotic model is still in an early stage. Manual cell seeding of the opposing compartments inevitably causes patterning inconsistency. In the follow-up studies, 3D printing technology can be used to generate complex diseased tissues which possess precise regional differences in cell types and mechanical properties.[56] With this approach, we could unprecedentedly create scar tissues of customizable shape, size, and composition to enable disease modeling of specific types of cardiomyopathies. This work only demonstrates preliminary drug screening results. Future optimally designed drug screening studies using multipronged approaches are required to test potential compounds and design effective treatment strategies. Further studies of dosage, delivery route, treatment onset, and length of administration will precisely dissect antifibrotic mechanisms and effects of the treatment.

METHODS

Biowire Chip Design and Fabrication. Photomasks for fabricating the tissue chip and the polymer wire were designed using AutoCAD as previously reported.[16,19] The master molds were fabricated by soft lithography using the negative photoresist SU-8(MICRO CHEM). Polydimethylsiloxane (PDMS) molds were made by replica molding from the SU-8 master molds. The PDMS mold for the chip fabrication was plasma bonded to a silicon wafer, and the features were hot embossed onto a polystyrene sheet. POMaC polymer wires were prepared from a prepolymer as previously described.[57] The PDMS mold for fabrication of the wires was pressed onto a glass slide, followed by the perfusion of POMaC prepolymer solution through the microchannels by capillary action. After UV cross-linking of the prepolymer wire and peeling off the PDMS, the POMaC wires were soaked in phosphate buffered saline to release them from the glass slide and were manually placed into the two parallel grooves patterned into the polystyrene sheet. Clear polyurethane 2-part adhesive (SP 1552-2, GS Polymers, Inc.) was used in a minimum quantity to fix the POMaC wires in place.

Generation of Fibrotic and Control Cardiac Tissues. Predominantly ventricular cardiomyocytes (CMs) were derived from the human induced pluripotent stem cell (hiPSC) line BJ1D using the monolayer differentiation protocols as previously described.[58] iCell cardiomyocytes were purchased from CDI and used according to the manufacturer's instructions. hiPSC-derived CMs were mixed with cardiac fibroblasts in 3:1 (normal) and 1:3 (fibrotic) cell number ratios, pelleted, and resuspended at a concentration of 5.5×10^7 cells/mL in the hydrogel. A fibrin/Matrigel hydrogel was prepared by combining the fibrinogen with Matrigel (BD Biosciences) in a 3:1 ratio. A volume of 0.5 μL of 25 IU/mL thrombin (Sigma-Aldrich) was added to each microwell prior to cell seeding. The cell−hydrogel suspension (2 μL per well) was seeded into the polystyrene microwells, to give a final seeding of 1.1×10^5 cells/microchamber. After 15 min of gelation at 37 °C, 15 mL of Induction 3 Medium (I3M) (StemPro-34 complete media, 20 mM HEPES, 1% GlutaMAX, 1% penicillin−streptomycin, Life Technologies; 213 μg/mL 2-phosphate ascorbic acid, Sigma-Aldrich) was added to the 10 cm dish. Aprotinin (Sigma-Aldrich) was added to the media at 10 μM. After seeding (day 0), the engineered cardiac tissues were cultured for 7 days to allow for remodeling and compaction around the POMaC wires. Daily bright field images of the tissues were taken using an Olympus CKX41 inverted microscope and CellSens software (Olympus Corporation). To generate integrated tissues, the aforementioned fibrotic and normal cell−hydrogel mixtures were pelleted and resuspended. One side of the Biowire II well was first seeded with normal cell suspension and left at the

DOI: 10.1021/acscentsci.9b00052
ACS Cent. Sci. 2019, 5, 1146−1158

room temperature for 10 min, followed by seeding on the other side with the fibrotic cell suspension. After seeding, tissues were cultured for 7 days to allow for remodeling and compaction around the POMaC wires.

Contractility Assessment and Force Measurement. On day 8 and weekly thereafter, 4× bright field movies were taken of spontaneous cardiac tissue beating and beating under stimulation at 1 Hz to record a contractile pattern and force displacement for the force calculation performed according to the calibration curves we published previously.[16] The minimum voltage/cm required to stimulate the synchronized contraction of the tissue (ET) and the maximum frequency the tissue could contract in response to the stimulation pulse at 2 times ET (MCR) were measured and recorded. POMaC is intrinsically fluorescent; hence, the deflection of the polymer wire due to the tissue contraction was isolated and tracked under blue fluorescent light. DAPI channel movies were taken to record the bending movement of the POMaC wire during tissue contraction from 1 to 6 Hz to measure the force−frequency relationship (FFR). After the tissue had been stimulated at 6 Hz for 20 s, stimulation was stopped for 10 s (rest period), and the stimulation was reinitiated at 1 Hz to measure PRP of the tissue. For the force calculation, blue channel image sequences were analyzed using a custom MatLab code that traced the maximum deflection of the POMaC wire. The average tissue width and width of the tissue on the polymer wire (Tw) were measured from still frames of the 4× bright field video of the tissue in the relaxed position. Total (at peak contraction) and passive (at rest) POMaC wire deflection was converted to force measurements (μN) using the standard forces curves.[16] The customized tips to match the Biowire tissue width in 3 different sizes were fabricated, by affixing a custom tip (0.5, 0.7, and 0.8 mm diameter) to a 0.1524 mm diameter tungsten probe to recapitulate the tissue diameter and curvature on the POMaC wire, as previously described.[16] The custom tips (half ellipse, 4:1 diameter ratio) were fabricated from an SU-8 master by soft lithography and were attached to the tungsten probe using an adhesive (T-GSG-01 Titan Gel). The experimental data, over the entire range, for each custom tip were fit to a third-degree polynomial equation, generating a force−displacement calibration curve for each custom probe tip. The final readouts for the total and passive force of tissue were then interpolated according to the Tw and custom tip sizes, as previously reported.[16] The active force was calculated as the difference between the total and passive force. The tissue cross-sectional area was measured at 3 different locations across the tissue. Then, the average cross-sectional area was calculated and used in the conversion of total active force (μN) produced by the entire tissue (calculated from the polymer wire displacement) to the average stress (μN/mm^2) exhibited by the tissue. The custom MatLab code was used to calculate the passive and active force. For the FFR measurements, normalized forces were calculated by dividing the active force measured at any given frequency to the active force of the same tissue paced at 1 Hz.

Electrical Stimulation. After 7 days of preculture, each strip of 8 Biowire II tissues was transferred to the electrical stimulation chamber, as previously reported.[16] On the basis of the electrical property assessment, the stimulation voltage was selected (1.5 times the average ET). All imaging was performed using an Olympus IX81 inverted fluorescent microscope and CellSens software (Olympus Corporation). Electrical stimulation was continued with weekly monitoring of ET, MCR, FFR, and PRP. I3M media was changed every week. Electrical stimulation started at 1 Hz on day 7, and the protocol of 1 Hz weekly step-up was used until the frequency reached 6 Hz. End point assessments were performed when a positive FFR (at least 1−3 Hz) was achieved. If a positive FFR was not observed once the tissues reached 6 Hz, stimulation continued at 6 Hz until a positive FFR was observed. The stimulation voltage was adjusted weekly to 1.5 times ET down to a minimum voltage of 3.5 V/cm. Control tissues were cultured without electrical stimulation.

Immunostaining and Confocal Microscopy. The tissues were fixed with 4% paraformaldehyde, permeablized by 0.25% Triton X-100, and blocked by 5% bovine serum albumin (BSA). Immunostaining was performed using the antibodies mouse anti-α-actinin (Abcam; 1:200), rabbit anti-SMA (Abcam, 1:200), Vimentin (Sigma, 1:200), mouse antitype I collagen (GeneTex, 1:200), and rabbit anti-connexin 43 (Cx-43) (Abcam; 1:200) and the secondary antibodies donkey antimouse-Alexa Fluor 488 (Abcam; 1:400) and donkey antirabbit-Alexa Fluor 594 (Life Technologies; 1:200). Phalloidin-Alexa Fluor 660 (Invitrogen; 1:200) was used to stain F-actin fibers. Conjugated vimentin-Cy3 (Sigma; 1:200) was used to stain for vimentin. Confocal microscopy images were obtained using an Olympus FluoView 1000 laser scanning confocal microscope (Olympus Corporation). Cardiomyocytes and fibroblasts were quantified by the average number of α-actinin or vimentin stained cells divided by the total cell number based on DAPI counterstain (n = 3). The 100 mM potassium chloride (Sigma) was used to relax the tissue prior to fixation for sarcomere length measurement. The respective sarcomere length in normal and fibrotic tissues stained with sarcomeric α-actinin was measured following imaging.

Second Harmonic Generation Imaging and Quantification. Biowires were fixed with 4% paraformaldehyde and imaged by an SHG laser scanning microscope (Zeiss LSM710 wo-Photon/Confocal microscope). The two-photon laser tuned to 860 nm was attached to the microscope and resulted in an SHG signal detectable at 475 nm. To ensure a consistent SHG signal and intrinsic fluorescence intensity, clear collagen morphology for quantitative analysis, and less photodamage of specimens, the detector offset and gain were optimized and held at a constant value for each region imaged. The quantification of collagen fibers was performed with ImageJ. A minimal threshold was set in the second harmonic signal. The threshold was maintained for all images across all conditions. The area of regions that was covered by the minimal threshold was calculated, and 3 images per sample were averaged together.

For SHG with the rat heart sections, sections were obtained in a previous study.[59] Lewis rats (200−250 g) were obtained from Charles River Laboratories (Saint-Constant, QC, Canada), and MI was generated under general anesthesia by performing left anterior descending artery ligation as previously described.[59] Three weeks after ligation, rats were assessed by echocardiography, and only those exhibiting 20−40% fractional shortening were included in the study. Paraffin embedding and sectioning was done on samples prepared as described above by the Pathology Research Program at the University Health Network. Sham and MI heart sections were blindly chosen for SHG imaging.

Intracellular Recording. Biowire II tissues were incubated in 35−37 °C Dulbecco's modified Eagle's medium (DMEM).

DOI: 10.1021/acscentsci.9b00052
ACS Cent. Sci. 2019, 5, 1146−1158

They were paced at 2× their excitation threshold. The movement of the tissues was minimized by 20 min treatment with 10 μ blebbistatin (Toronto research chemicals) to eliminate motion artifacts. The action potential was recorded with a high impedance microelectrode of 60−90 MΩ filled with 3 M KCl. Microelectrodes were connected to a Duo 773 electrometer (World Precision Instrument). The recording was performed on current clamp mode at 10 kHz, and signals were analyzed by Clampfit 10 (Axon instrument).

Optical Mapping. Tissues were treated with 2 μM voltage sensitive dye, Di-4-ANEPPS (Invitrogen) in DMEM for 30 min at room temperature. The tissues were paced at 1.5−2 Hz with a Pulsar 6i Stimulator (FHC, Inc.) at 2× their excitation threshold. Tissue contraction was stopped by 20 min treatment with 10 μM blebbistatin. Dye fluorescence was recorded on an MVX-10 Olympus fluorescence microscope (Olympus Corporation) equipped with a charged coupled device (CCD) (Cascade 128, Photometrics). The 1 cm sensor had 128 × 128 pixel resolution. Recordings were performed at 500 frames/s with 0 exposure time. Maps were generated by scroll software.

Mechanical Testing. The elastic modulus of the tissues was tested by stretching tests with MicroSquisher (CellScale) (n = 9) using the 0.2 mm diameter tungsten probe. During the test, the tissues were affixed to a 10 cm dish in culture media. A micropin was used to anchor one side of the tissue to the plate. The probe tip was placed at the other end of the tissue, and the tissue was subsequently stretched in the longitudinal direction at a velocity of 2.5 μm/s. Force, probe displacement, and time were recorded. The tissue length and cross-section were measured to calculate strain and stress. Young's modulus values of samples were calculated from the initial linear region, i.e., up to 15% strain range for both normal and fibrotic tissues, on the basis of the sample's linear elastic region of the curves, using a using linear least-squares fit.

Calcium Transient Recording. To investigate the relative changes of intracellular calcium concentration, tissues were incubated with the calcium dye Fluo-4 NW (Thermo Fisher) for 30 min at 37 °C prior to testing. For measuring excitation−contraction coupling, calcium transients and contractility readouts were obtained from the same tissue simultaneously in the same frames. The testing process was performed using the green light channel (λ_{ex} = 490 nm, λ_{em} = 525 nm) and 4× magnification. The ImageJ software (NIH) Stacks plugin was used to determine the average intensity of a region of interest in the tissue located at a distance from the POMaC wire, wherein the movement artifacts were minimal. The ratio of peak tissue fluorescence intensity to baseline intensity, dF/F0, was calculated to determine the relative changes in intracellular calcium in fibrotic and control models. The contractile measurements were extracted from the green channel videos using a modified version of the ImageJ SpotTracker plugin. For the consecutive force and calcium transient readouts, contractile measurements were extracted from the blue channel as described before. For the synchronous readouts, the contractile measurements were extracted from the green channel videos using a modified version of the ImageJ SpotTracker plugin.

Scar-in-a-Jar Assay. Normal human dermal fibroblasts (NHDFs) from juvenile foreskin (j-NHDFs, Promocell C-12300) were plated on 96-well plates at 6000 cells per well in fibroblast basal medium (FBM, Lonza CC-3130) containing 2% fetal bovine serum (FBS) and cultured under 5% CO_2 at 37°C. After 24 h, cells were switched to FBM containing 0.5% FBS, containing 25 mg/mL Ficoll 400 and 100 μM L-ascorbic acid 2-phosphate (Sigma A8960). Small-molecule treatments were applied at the same time as Ficoll 400. Three inhibitors of proprotein convertase were p-guanidinomethyl-phenylacetyl-Arg-Val-Arg-4-amidinobenzylamide (PCi, Calbiochem 537076), dec-RVKR-cmk (FiI, Tocris Bioscience 3501), and hexa-D-arginine amide (FiII, Tocris Bioscience 4711). After 3 days of biophysical crowding, cells were fixed in ice-cold MeOH for 10 min at 4°C, blocked in 3% BSA for 30 min, and incubated in 1/500 mouse monoclonal anticollagen type 1 (C2456, Sigma), 1/500 rabbit polyclonal antifibronectin (F3648, Sigma), or 1/100 rabbit polyclonal anti-TGN46 (13573-1-AP, Proteintech) overnight. Subsequently, goat antimouse IgG-Alexa488 and goat antirabbit IgG-Alexa647 (A-11001 and A-21245, respectively, Life Technologies) were used at 1/400 and counterstained with Hoechst for 1.5 h. Signals of collagen type I and fibronectin were imaged on the Operetta System (PerkinElmer).

Drug Testing. Proprotein convertase inhibitor Calbiochem 537076 (PCI) was prepared in dimethyl sulfoxide (DMSO) solution as previously reported.[59] A working concentration of 2.5 μM was achieved by diluting the stock in maintenance medium. Two screening timelines, late treatment after tissue maturation, and early treatment upon seeding were used to treat the tissues with compounds and DMSO controls.

Statistical Analysis. Statistical analysis was performed using Prism 7.0 software. Differences between experimental groups were analyzed by Student's t test (two groups) or one-way ANOVA (more than two groups). Experiments with two or three different variables were analyzed with two-way or three-way ANOVA. The normality test (Shapiro−Wilk) and pairwise multiple comparison procedures (Tukey's post hoc method or Holm−Sidak method) were used for one-way ANOVA and two-way ANOVA tests. The statistical significance was accepted at the $p < 0.05$ level and indicated in figures as * $p < 0.05$, ** $p < 0.01$, and *** $p < 0.001$. The Z-factor used in Figure S3 was defined as $1 - [(3(\sigma p + \sigma n))/|\mu p - \mu n|]$, in terms of the means (μ) and standard deviations (σ).

Safety Statement. No unexpected or unusually high safety hazards were encountered.

■ ASSOCIATED CONTENT

Supporting Information

The Supporting Information is available free of charge on the ACS Publications website at DOI: 10.1021/acscentsci.9b00052.

Figures on FFR analysis, tissue assessment with iCells, action potential profiles, additional drug screening data, additional immunostaining images, and comparison study of rat heart collagen deposition (PDF)

■ AUTHOR INFORMATION

Corresponding Author

*E-mail: m.radisic@utoronto.ca.

ORCID

Erika Yan Wang: 0000-0002-1634-7493

Milica Radisic: 0000-0003-1249-4135

Author Contributions

○N.R. and Y.Z. contributed equally to this work as second authors. Conceptualization was performed by E.Y.W., Y.Z., N.R., A.L., S.B., and M.R. Methodology was performed by E.Y.W., Y.Z., N.R., and M.R. Formal analysis was performed by

DOI: 10.1021/acscentsci.9b00052
ACS Cent. Sci. 2019, 5, 1146−1158

E.Y.W., Y.Z., N.R., and D.J. Investigation was performed by E.Y.W., Y.Z., and N.R. Resources were handled by P.H.B., M.R., B.F.L.L., R.X.L., L.D.H., and E.K.W. The writing of the original draft was performed by E.Y.W. The writing, review, and editing were performed by E.Y.W. and M.R. Visualization was performed by E.Y.W., N.R., and A.L. Supervision was performed by M.R. Funding acquisition was handled by S.B. and M.R.

Notes

The authors declare the following competing financial interest(s): Y.Z. and M.R. are co-founders of TARA Biosystems Inc. and hold equity in this company. TARA Biosystems Inc. uses the Biowire II technology described in this manuscript for commercial applications. All other authors have no conflicts of interest.

■ ACKNOWLEDGMENTS

This work was funded by the Canadian Institutes of Health Research (CIHR) Operating Grants (MOP-126027 and MOP-137107), Natural Sciences and Engineering Research Council of Canada (NSERC) Discovery Grant (RGPIN 326982-10), NSERC−CIHR Collaborative Health Research Grant (CHRP 493737-16), and National Institutes of Health Grant 2R01 HL076485. M.R. was supported by NSERC Steacie Fellowship and Canada Research Chair. E.Y.W. was supported by Alexander Graham Bell Canada Graduate Scholarship−Doctoral Award (CGS−D). Y.Z. was supported by NSERC Postgraduate Fellowship and Ted Rogers Center for Heart Research Doctoral Award.

■ REFERENCES

(1) Kong, P.; Christia, P.; Frangogiannis, N. G. The pathogenesis of cardiac fibrosis. *Cell. Mol. Life Sci.* **2014**, *71*, 549−574.

(2) Krenning, G.; Zeisberg, E. M.; Kalluri, R. The origin of fibroblasts and mechanism of cardiac fibrosis. *J. Cell. Physiol.* **2010**, *225*, 631−637.

(3) Leask, A. Getting to the heart of the matter: new insights into cardiac fibrosis. *Circ. Res.* **2015**, *116*, 1269−1276.

(4) Lajiness, J. D.; Conway, S. J. Origin, development, and differentiation of cardiac fibroblasts. *J. Mol. Cell. Cardiol.* **2014**, *70*, 2−8.

(5) Fan, Z.; Guan, J. Antifibrotic therapies to control cardiac fibrosis. *Biomaterials research* **2016**, *20*, 13−13.

(6) Jousset, F.; Maguy, A.; Rohr, S.; Kucera, J. P. Myofibroblasts electrotonically coupled to cardiomyocytes alter conduction: insights at the cellular level from a detailed in silico tissue structure model. *Front. Physiol.* **2016**, *7*, 496.

(7) Vasquez, C.; Morley, G. E. The origin and arrhythmogenic potential of fibroblasts in cardiac disease. *Journal of Cardiovascular Translational Research* **2012**, *5*, 760−767.

(8) Conant, G.; Lai, B. F. L.; Lu, R. X. Z.; Korolj, A.; Wang, E. Y.; Radisic, M. High-content assessment of cardiac function using heart-on-a-chip devices as drug screening model. *Stem Cell Rev. and Rep* **2017**, *13*, 335−346.

(9) Chen, C.; Peng, Y.; Wang, Z.; Fish, P.; Kaar, J.; Koepsel, R.; Russell, A.; Lareu, R.; Raghunath, M. The scar-in-a-jar: studying potential antifibrotic compounds from the epigenetic to extracellular level in a single well. *Br. J. Pharmacol.* **2009**, *158*, 1196−1209.

(10) Ahadian, S.; Civitarese, R.; Bannerman, D.; Mohammadi, M. H.; Lu, R.; Wang, E.; Davenport-Huyer, L.; Lai, B.; Zhang, B.; Zhao, Y.; Mandla, S.; Korolj, A.; Radisic, M. Organ-on-a-chip platforms: a convergence of advanced materials, cells, and microscale technologies. *Adv. Healthcare Mater.* **2018**, *7*, 1700506.

(11) Savoji, H.; Mohammadi, M. H.; Rafatian, N.; Toroghi, M. K.; Wang, E. Y.; Zhao, Y.; Korolj, A.; Ahadian, S.; Radisic, M. Cardiovascular disease models: A game changing paradigm in drug discovery and screening. *Biomaterials* **2019**, *198*, 3−26.

(12) Sadeghi, A. H.; Shin, S. R.; Deddens, J. C.; Fratta, G.; Mandla, S.; Yazdi, I. K.; Prakash, G.; Antona, S.; Demarchi, D.; Buijsrogge, M. P.; Sluijter, J. P. G.; Hjortnaes, J.; Khademhosseini, A. Engineered 3D cardiac fibrotic tissue to study fibrotic remodeling. *Adv. Healthcare Mater.* **2017**, *6*, 1601434.

(13) Spencer, T. M.; Blumenstein, R. F.; Pryse, K. M.; Lee, S.-L.; Glaubke, D. A.; Carlson, B. E.; Elson, E. L.; Genin, G. M. Fibroblasts slow conduction velocity in a reconstituted tissue model of fibrotic cardiomyopathy. *ACS Biomater. Sci. Eng.* **2017**, *3*, 3022−3028.

(14) Asmani, M.; Velumani, S.; Li, Y.; Wawrzyniak, N.; Hsia, I.; Chen, Z.; Hinz, B.; Zhao, R. Fibrotic microtissue array to predict anti-fibrosis drug efficacy. *Nat. Commun.* **2018**, *9*, 2066.

(15) Nunes, S. S.; Miklas, J. W.; Liu, J.; Aschar-Sobbi, R.; Xiao, Y.; Zhang, B.; Jiang, J.; Massé, S.; Gagliardi, M.; Hsieh, A.; Thavandiran, N.; Laflamme, M. A.; Nanthakumar, K.; Gross, G. J.; Backx, P. H.; Keller, G.; Radisic, M. Biowire: a platform for maturation of human pluripotent stem cell−derived cardiomyocytes. *Nat. Methods* **2013**, *10*, 781−787.

(16) Zhao, Y.; Rafatian, N.; Feric, N. T.; Cox, B. J.; Aschar-Sobbi, R.; Wang, E. Y.; Aggarwal, P.; Zhang, B.; Conant, G.; Ronaldson-Bouchard, K.; Pahnke, A.; Protze, S.; Lee, J. H.; Davenport Huyer, L.; Jekic, D.; Wickeler, A.; Naguib, H. E.; Keller, G. M.; Vunjak-Novakovic, G.; Broeckel, U.; Backx, P. H.; Radisic, M. A platform for generation of chamber-specific cardiac tissues and disease modeling. *Cell* **2019**, *176*, 913−927.

(17) Sluijter, J. P. G.; Verloop, R. E.; Pulskens, W. P. C.; Velema, E.; Grimbergen, J. M.; Quax, P. H.; Goumans, M.-J.; Pasterkamp, G.; de Kleijn, D. P. V. Involvement of furin-like proprotein convertases in the arterial response to injury. *Cardiovasc. Res.* **2005**, *68*, 136−143.

(18) Ichiki, T.; Boerrigter, G.; Huntley, B. K.; Sangaralingham, S. J.; McKie, P. M.; Harty, G. J.; Harders, G. E.; Burnett, J. C. Differential expression of the pro-natriuretic peptide convertases Corin and furin in experimental heart failure and atrial fibrosis. *American Journal of Physiology-Regulatory, Integrative and Comparative Physiology* **2013**, *304*, R102−R109.

(19) Zhao, Y.; Wang, E. Y.; Davenport, L. H.; Liao, Y.; Yeager, K.; Vunjak-Novakovic, G.; Radisic, M.; Zhang, B. A multimaterial microphysiological platform enabled by rapid casting of elastic microwires. *Adv. Healthcare Mater.* **2019**, *8*, 1801187.

(20) Ronaldson-Bouchard, K.; Ma, S. P.; Yeager, K.; Chen, T.; Song, L.; Sirabella, D.; Morikawa, K.; Teles, D.; Yazawa, M.; Vunjak-Novakovic, G. Advanced maturation of human cardiac tissue grown from pluripotent stem cells. *Nature* **2018**, *556*, 239−243.

(21) Korolj, A.; Wang, E. Y.; Civitarese, R. A.; Radisic, M. Biophysical stimulation for in vitro engineering of functional cardiac tissues. *Clin. Sci.* **2017**, *131*, 1393−1404.

(22) Fomovsky, G. M.; Rouillard, A. D.; Holmes, J. W. Regional mechanics determine collagen fiber structure in healing myocardial infarcts. *J. Mol. Cell. Cardiol.* **2012**, *52*, 1083−1090.

(23) Besser, R. R.; Ishahak, M.; Mayo, V.; Carbonero, D.; Claure, I.; Agarwal, A. Engineered microenvironments for maturation of stem cell derived cardiac myocytes. *Theranostics* **2018**, *8*, 124−140.

(24) Bott, K.; Upton, Z.; Schrobback, K.; Ehrbar, M.; Hubbell, J. A.; Lutolf, M. P.; Rizzi, S. C. The effect of matrix characteristics on fibroblast proliferation in 3D gels. *Biomaterials* **2010**, *31*, 8454−8464.

(25) Jackman, C. P.; Carlson, A. L.; Bursac, N. Dynamic culture yields engineered myocardium with near-adult functional output. *Biomaterials* **2016**, *111*, 66−79.

(26) Mannhardt, I.; Breckwoldt, K.; Letuffe-Brenière, D.; Schaaf, S.; Schulz, H.; Neuber, C.; Benzin, A.; Werner, T.; Eder, A.; Schulze, T.; Klampe, B.; Christ, T.; Hirt, M. N.; Huebner, N.; Moretti, A.; Eschenhagen, T.; Hansen, A. Human engineered heart tissue: analysis of contractile force. *Stem Cell Rep.* **2016**, *7*, 29−42.

(27) Riegler, J.; Tiburcy, M.; Ebert, A.; Tzatzalos, E.; Raaz, U.; Abilez Oscar, J.; Shen, Q.; Kooreman Nigel, G.; Neofytou, E.; Chen Vincent, C.; Wang, M.; Meyer, T.; Tsao Philip, S.; Connolly Andrew, J.; Couture Larry, A.; Gold Joseph, D.; Zimmermann Wolfram, H.;

DOI: 10.1021/acscentsci.9b00052
ACS Cent. Sci. 2019, 5, 1146−1158

Wu Joseph, C. Human engineered heart muscles engraft and survive long term in a rodent myocardial infarction model. *Circ. Res.* **2015**, *117*, 720−730.
(28) Jacot, J. G.; Martin, J. C.; Hunt, D. L. Mechanobiology of cardiomyocyte development. *J. Biomech.* **2010**, *43*, 93−98.
(29) van Spreeuwel, A.; et al. The relevance of extracellular matrix structure and composition in engineering the diseased cardiac microenvironment. *OA Tissue Engineering* **2014**, *18*, 2.
(30) Røe, Å. T.; Aronsen, J. M.; Skårdal, K.; Hamdani, N.; Linke, W. A.; Danielsen, H. E.; Sejersted, O. M.; Sjaastad, I.; Louch, W. E. Increased passive stiffness promotes diastolic dysfunction despite improved Ca2+ handling during left ventricular concentric hypertrophy. *Cardiovasc. Res.* **2017**, *113*, 1161−1172.
(31) Parker, M. W.; Rossi, D.; Peterson, M.; Smith, K.; Sikström, K.; White, E. S.; Connett, J. E.; Henke, C. A.; Larsson, O.; Bitterman, P. B. Fibrotic extracellular matrix activates a profibrotic positive feedback loop. *J. Clin. Invest.* **2014**, *124*, 1622−1635.
(32) Shi, Y.; Zhang, J.; Xu, W.; Yi, J.; Li, Y.; Chen, Y. The correlation of TGFβ1 gene polymorphisms with congenital heart disease susceptibility. *Gene* **2019**, *686*, 160−163.
(33) Tsuda, T. Extracellular interactions between fibulins and transforming growth factor (TGF)-β in physiological and pathological conditions. *Int. J. Mol. Sci.* **2018**, *19*, 2787.
(34) Xu, Q.; Norman, J. T.; Shrivastav, S.; Lucio-Cazana, J.; Kopp, J. B. In vitro models of TGF-β-induced fibrosis suitable for high-throughput screening of antifibrotic agents. *American Journal of Physiology-Renal Physiology* **2007**, *293*, F631−F640.
(35) Dobaczewski, M.; Chen, W.; Frangogiannis, N. G. Transforming growth factor (TGF)- β signaling in cardiac remodeling. *J. Mol. Cell. Cardiol.* **2011**, *51*, 600−606.
(36) Kohl, P.; Gourdie, R. G. Fibroblast-myocyte electrotonic coupling: does it occur in native cardiac tissue? *J. Mol. Cell. Cardiol.* **2014**, *70*, 37−46.
(37) Mendonca Costa, C.; Plank, G.; Rinaldi, C. A.; Niederer, S. A.; Bishop, M. J. Modeling the electrophysiological properties of the infarct border zone. *Front. Physiol.* **2018**, *9*, 356.
(38) Piacentino, V.; Weber, C. R.; Chen, X.; Weisser-Thomas, J.; Margulies, K. B.; Bers, D. M.; Houser, S. R. Cellular basis of abnormal calcium transients of failing human ventricular myocytes. *Circ. Res.* **2003**, *92*, 651−658.
(39) Ramanathan, C.; Jia, P.; Ghanem, R.; Ryu, K.; Rudy, Y. Activation and repolarization of the normal human heart under complete physiological conditions. *Proc. Natl. Acad. Sci. U. S. A.* **2006**, *103*, 6309.
(40) Li, G.-R.; Feng, J.; Yue, L.; Carrier, M. Transmural heterogeneity of action potentials andI to1 in myocytes isolated from the human right ventricle. *American Journal of Physiology-Heart and Circulatory Physiology* **1998**, *275*, H369−H377.
(41) Shattock, M. J.; Winter, J. Geometrical considerations in cardiac electrophysiology and arrhythmogenesis. *EP Europace* **2016**, *18*, 320−331.
(42) Jacquemet, V. A simple analytical model of action potential duration profile in electrotonically-coupled cells. *Math. Biosci.* **2016**, *272*, 92−99.
(43) Aguilar, M.; Qi, X. Y.; Huang, H.; Comtois, P.; Nattel, S. Fibroblast electrical remodeling in heart failure and potential effects on atrial fibrillation. *Biophys. J.* **2014**, *107*, 2444−2455.
(44) Choudhury, S.; Bae, S.; Ke, Q.; Lee, J. Y.; Singh, S. S.; St-Arnaud, R.; Monte, F. d.; Kang, P. M. Abnormal calcium handling and exaggerated cardiac dysfunction in mice with defective vitamin D signaling. *PLoS One* **2014**, *9*, e108382.
(45) Endoh, M. Force−frequency relationship in intact mammalian ventricular myocardium: physiological and pathophysiological relevance. *Eur. J. Pharmacol.* **2004**, *500*, 73−86.
(46) Pieske, B.; Hasenfuss, G.; Holubarsch, C.; Schwinger, R.; Böhm, M.; Just, H. In Alterations of the force-frequency relationship in the failing human heart depend on the underlying cardiac disease. *Cellular and Molecular Alterations in the Failing Human Heart, Heidelberg* **1992**, 213−221.
(47) Anderson, P. A. W.; Manring, A.; Johnson, E. A. Force-frequency relationship. *Circ. Res.* **1973**, *33*, 665−671.
(48) Schwinger, R. H.; Böhm, M.; Koch, A.; Erdmann, E. Force-frequency relation in human heart failure. *Circulation* **1992**, *86*, 2017−2018.
(49) Gerbin, K. A.; Yang, X.; Murry, C. E.; Coulombe, K. L. K. Enhanced electrical integration of engineered human myocardium via intramyocardial versus epicardial delivery in infarcted rat hearts. *PLoS One* **2015**, *10*, e0131446.
(50) Bucciarelli-Ducci, C.; Baritussio, A.; Auricchio, A. Cardiac MRI anatomy and function as a substrate for arrhythmias. *EP Europace* **2016**, *18*, iv130−iv135.
(51) Prinz, C.; Schwarz, M.; Ilic, I.; Laser, K. T.; Lehmann, R.; Prinz, E.-M.; Bitter, T.; Vogt, J.; van Buuren, F.; Bogunovic, N.; Horstkotte, D.; Faber, L. Myocardial fibrosis severity on cardiac magnetic resonance imaging predicts sustained arrhythmic events in hypertrophic cardiomyopathy. *Can. J. Cardiol.* **2013**, *29*, 358−363.
(52) DiMasi, J. A. The value of improving the productivity of the drug development process faster times and better decisions. *PharmacoEconomics* **2002**, *20*, 1−10.
(53) Conant, G.; Ahadian, S.; Zhao, Y.; Radisic, M. Kinase inhibitor screening using artificial neural networks and engineered cardiac biowires. *Sci. Rep.* **2017**, *7*, 11807.
(54) Torrisi, S. E.; Pavone, M.; Vancheri, A.; Vancheri, C. When to start and when to stop antifibrotic therapies. *European Respiratory Review* **2017**, *26*, 170053.
(55) Hinz, B.; Phan, S. H.; Thannickal, V. J.; Galli, A.; Bochaton-Piallat, M.-L.; Gabbiani, G. The myofibroblast: one function, multiple origins. *Am. J. Pathol.* **2007**, *170*, 1807−1816.
(56) Kang, H.-W.; Lee, S. J.; Ko, I. K.; Kengla, C.; Yoo, J. J.; Atala, A. A 3D bioprinting system to produce human-scale tissue constructs with structural integrity. *Nat. Biotechnol.* **2016**, *34*, 312.
(57) Locke, D. H.; Miles, M.; Yimu, Z.; Yun, X.; Genevieve, C.; Anastasia, K.; Milica, R. Biomaterial based cardiac tissue engineering and its applications. *Front. Bioeng. Biotechnol.* **2016**, *10*, 034004.
(58) Lian, X.; Hsiao, C.; Wilson, G.; Zhu, K.; Hazeltine, L. B.; Azarin, S. M.; Raval, K. K.; Zhang, J.; Kamp, T. J.; Palecek, S. P. Robust cardiomyocyte differentiation from human pluripotent stem cells via temporal modulation of canonical Wnt signaling. *Proc. Natl. Acad. Sci. U. S. A.* **2012**, *109*, E1848−57.
(59) Chiu, L. L. Y.; Reis, L. A.; Momen, A.; Radisic, M. Controlled release of thymosin β4 from injected collagen−chitosan hydrogels promotes angiogenesis and prevents tissue loss after myocardial infarction. *Regener. Med.* **2012**, *7*, 523−533.

DOI: 10.1021/acscentsci.9b00052
ACS Cent. Sci. 2019, 5, 1146−1158